Volumetric Color-Texture Representation for Colorectal Polyp Classification in Histopathology Images

Ricardo T. Fares[a] and Lucas C. Ribas[b]
São Paulo State University, Institute of Biosciences, Humanities and Exact Sciences, São José do Rio Preto, SP, Brazil
{rt.fares, lucas.ribas}@unesp.br

Keywords: Color-Texture, Texture Representation Learning, Randomized Neural Network.

Abstract: With the growth of real-world applications generating numerous images, analyzing color-texture information has become essential, especially when spectral information plays a key role. Currently, many randomized neural network texture-based approaches were proposed to tackle color-textures. However, they are integrative approaches or fail to achieve competitive processing time. To address these limitations, this paper proposes a single-parameter color-texture representation that captures both spatial and spectral patterns by sliding volumetric (3D) color cubes over the image and encoding them with a Randomized Autoencoder (RAE). The key idea of our approach is that simultaneously encoding both color and texture information allows the autoencoder to learn meaningful patterns to perform the decoding operation. Hence, we employ as representation the flattened decoder's learned weights. The proposed approach was evaluated in three color-texture benchmark datasets: USPtex, Outex, and MBT. We also assessed our approach in the challenging and important application of classifying colorectal polyps. The results show that the proposed approach surpasses many literature methods, including deep convolutional neural networks. Therefore, these findings indicate that our representation is discriminative, showing its potential for broader applications in histological images and pattern recognition tasks.

1 INTRODUCTION

The advancement of numerous image acquisition techniques has continuously enabled various real-world applications to acquire colored images. Largely, several of these applications, such as image retrieval (Liu and Yang, 2023), face recognition (Li et al., 2024), defect recognition (Su et al., 2024), and medical diagnosis (Rangaiah et al., 2025) rely on texture descriptors. Texture description of an image consists in leveraging one of the most important low-level visual cues, the texture, to obtain a sequence of real numbers describing the image with the purpose of performing pattern recognition tasks.

In this context, to enable the recognition of texture images, several texture descriptors have been developed and advanced over the years through techniques such as those based on local binary patterns (Ojala et al., 2002b; Guo et al., 2010; Hu et al., 2024), which encode pixel neighborhoods using the central pixel luminance as a threshold; graph-based methods (Backes et al., 2013; Scabini et al., 2019), which apply complex network theory to describe structural patterns in images using graph measures; and mathematical approaches that used the Bouligand-Minkowski fractal dimension (Backes et al., 2009). Although these methods are highly significant as they lay the foundation for the development of newer and more powerful approaches, they may fail to achieve strong performance on more complex images, as those may not be adequately described using only textural attributes.

In this sense, with the increasing attention of the research community in deep-learning and with the outstanding results achieved by AlexNet (Krizhevsky et al., 2012) in the ImageNet (Deng et al., 2009) challenge, there was a shift in focus to learning-based strategies, leading to the development of various CNN architectures, such as the VGG (Simonyan and Zisserman, 2014), ResNet (He et al., 2016) and DenseNet (Huang et al., 2017) families.

Nevertheless, deep neural networks pose some challenges, such as their need for large training data and significant computational cost due to the training of their large number of parameters. In relation to large training data issues, numerous recent method-

[a] https://orcid.org/0000-0001-8296-8872
[b] https://orcid.org/0000-0003-2490-180X

Fares, R. T. and Ribas, L. C.
Volumetric Color-Texture Representation for Colorectal Polyp Classification in Histopathology Images.
DOI: 10.5220/0013315800003912
Paper published under CC license (CC BY-NC-ND 4.0)
In *Proceedings of the 20th International Joint Conference on Computer Vision, Imaging and Computer Graphics Theory and Applications (VISIGRAPP 2025) - Volume 3: VISAPP*, pages 210-221
ISBN: 978-989-758-728-3; ISSN: 2184-4321
Proceedings Copyright © 2025 by SCITEPRESS – Science and Technology Publications, Lda.

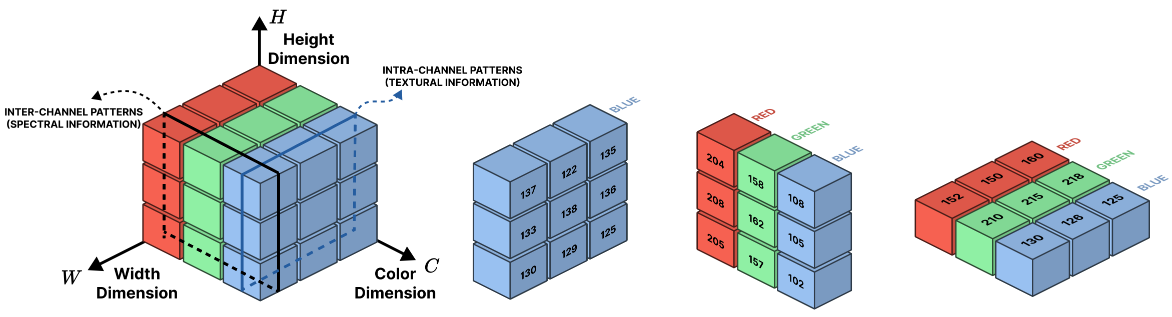

(a) Three-dimensional Visualization of the 3D Color Cube

(b) Textural Patterns in the HW plane. (Intra-channel)

(c) Color Patterns in the HC plane. (Inter-channel)

(d) Color Patterns in the WC plane. (Inter-channel)

Figure 1: Illustration of the 3D color cubes used to capture spatial and cross-channel color information in the color-texture image. (a) Three-dimensional view of the 3D color cube. (b) Extracted textural patterns in the HW plane. (c) Color patterns observed in the HC plane. (d) Color patterns observed in the WC plane.

ologies apply data augmentation. However, data augmentation must be carefully selected to not alter the sample label (Wang et al., 2021). On the other hand, although significant computational cost can be softened by using model compression through quantization or pruning, there may be some loss of accuracy during training (Marinó et al., 2023).

In this sense, many recent texture representation methods used randomized neural networks (Sá Junior and Backes, 2016; Ribas et al., 2024a; Fares et al., 2024). These networks offer simplicity, low computational costs, and have proven to obtain satisfactory results in pattern recognition applications. In these studies, the authors train a randomized neural network for each image and conduct a post-processing of the learned weights of the randomized neural network, which carries valuable information. Despite achieving good results, many color-texture representation methods focus on spatial patterns or apply separate grayscale analysis to each channel, overlooking spectral and cross-channel information, thus losing valuable color details. Furthermore, those that perform spatial-spectral analysis fail in achieving competitive feature extraction processing time.

To address these limitations, in this paper, we propose a fast single-parameter color-texture representation based on a randomized autoencoder that simultaneously encodes texture and color information (spatio-spectral) using volumetric (3D) color cubes. Initially, for a given 3-channel we assemble the input feature matrix by flattening 3D color cubes of dimension $3 \times 3 \times 3$ over the entire image (Fig. 1), capturing both spatio and spectral information. Following this, we apply this feature matrix of a single image to a randomized autoencoder that randomly projects the input data into another dimensional space, and learns how to reconstruct them back to the input space, thereby learning the meaningful textural and color characteristics to perform it. Thus, we use as color-texture representation the flattening of the decoder's learned weights of the randomized autoencoder. Overall, the major contributions of our work are:

- Simple, fast and low cost approach that learns the representation using a single instance due to use of randomized autoencoders.
- A texture representation that simultaneously captures both texture and color patterns.
- A color-texture representation that outperforms several texture-only literature methods in the application of classifying colorectal polyps.

This paper is organized as follows: Section 2 presents the proposed color-texture representation approach. Section 3 presents the experimental setup, the results, and comparisons with other literature methods, and Section 4 concludes this paper.

2 PROPOSED APPROACH

2.1 Randomized Neural Networks

Randomized neural networks (RNN) consist of a single fully-connected hidden layer, with the weights randomly generated from a probability distribution (e.g. normal or uniform) (Huang et al., 2006; Pao and Takefuji, 1992; Pao et al., 1994; Schmidt et al., 1992). Their simplicity arises from the use of a single hidden layer, and the learning phase is efficient due to the output layer weights being computed via a closed-form solution. The network's primary goal is to non-linearly random project the input data into another dimensional space to enhance the linear separability of the data, as stated in Cover's theorem (Cover, 1965). The weights of the output layer are then learned by

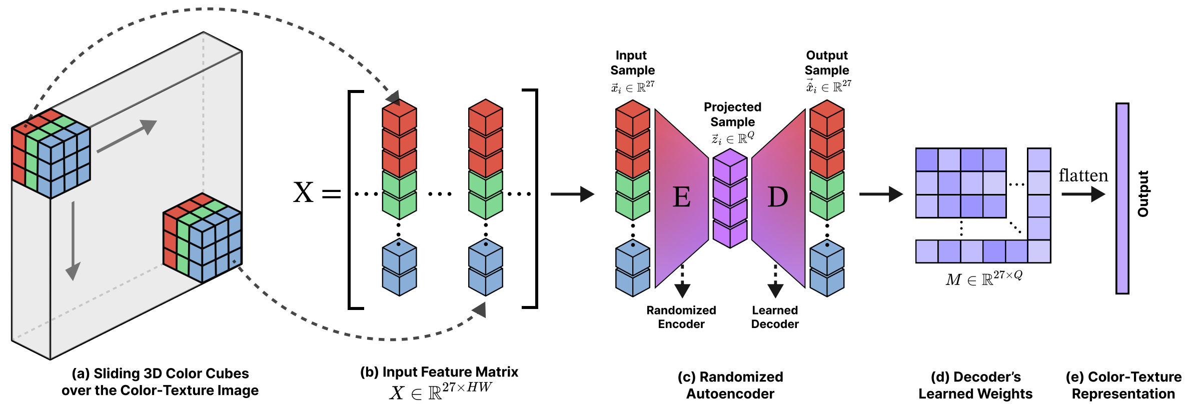

X =
Input Sample
$\vec{x}_i \in \mathbb{R}^{27}$
Projected Sample
$\vec{z}_i \in \mathbb{R}^{Q}$
Output Sample
$\hat{\vec{x}}_i \in \mathbb{R}^{27}$
E
D
Randomized Encoder
Learned Decoder
$M \in \mathbb{R}^{27\times Q}$
flatten
Output
(a) Sliding 3D Color Cubes over the Color-Texture Image
(b) Input Feature Matrix $X \in \mathbb{R}^{27\times HW}$
(c) Randomized Autoencoder
(d) Decoder's Learned Weights
(e) Color-Texture Representation

Figure 2: Illustration of the proposed color-texture methodology. (a) Sliding 3D color cubes over the color-texture image to build the input feature matrix. (b) The input feature matrix. (c) Randomized autoencoder to randomly project this matrix. (d) Decoder's learned weights. (e) Proposed color-texture representation.

fitting these linearly enhanced data using the least-squares method.

Formally, let $X \in \mathbb{R}^{p\times N}$ and $Y \in \mathbb{R}^{r\times N}$ be the input and output feature matrices, respectively. The input feature matrix is composed by N input feature vectors of dimension p, whereas the output feature matrix consists of N output feature vectors of dimension r. Subsequently, a probability distribution $p(\boldsymbol{x})$ is employed to generate the random weight matrix $W \in \mathbb{R}^{Q\times(p+1)}$, with the first column being the bias' weights, and where Q is the number of neurons in the hidden layer, or more specifically the dimension of the latent space.

Following this, we append a value -1 at the top of every column of X, linking the input feature vectors with the bias' weights. From this, the randomly projected input feature vectors can be computed by $Z = \phi(WX)$, where each column of Z consists of the projected feature vector, and ϕ is the sigmoid function. After obtaining the projected matrix Z, a -1 is appended to the top of each projected feature vector to connect to the bias weight of the output neurons.

Hence, the output layer weights (M) of the randomized neural network are computed using the following closed-form solution, which consists in a brief sequence of matrix operations:

$$M = YZ^T(ZZ^T + \lambda I)^{-1}, \qquad (1)$$

where the term $(ZZ^T + \lambda I)^{-1}$ represents the regularized Moore-Penrose pseudoinverse (Moore, 1920; Penrose, 1955) with Tikhonov's regularization (Tikhonov, 1963; Calvetti et al., 2000). This regularization is used to avoid issues related to the inversion of near-singular matrices. Finally, the randomized neural network may be employed as a randomized autoencoder (RAE) by setting $Y = X$.

2.2 VCTex: Volumetric Color-Texture Representation

In this paper, we propose to use as color-texture representation the flattened decoder's learned weights of a randomized autoencoder trained with simultaneous key information of color and textural patterns. These patterns are extracted using 3D color cubes that slide across the color-texture image, effectively capturing the color-textural information.

To build the color-texture representation, we first build the input feature matrix X. For this, let $I \in \mathbb{R}^{3\times H\times W}$ be any RGB image, we assemble X by flattening 3D cubes of size $3\times3\times3$ that slide over each pixel in the green channel and horizontally concatenate them. Positioning the cube in the green channel allows us to capture information from both red and blue channels. Consequently, each cube captures spatial patterns of each channel (each 3×3 window along the color depth) as well as cross-channel color (spectral) information, as illustrated in Figure 1.

After assembling the input feature matrix, we build the random weight matrix, W, to encode the input data. To ensure that our method consistently produces the same color-texture representation for the same image on every run, the random weights are kept fixed, ensuring reproducibility. To this end, we employ the Linear Congruent Generator (LCG) to obtain pseudorandom values for the matrix W using the recurrent formula: $V(n+1) = (aV(n)+b) \mod c$, where V has length $\ell = Q\cdot(p+1)$, and initial parameters set to $V(0) = \ell+1, a = \ell+2, b = \ell+3$, and $c = \ell^2$. Following this, V is standardized, and W results from turning the vector V into a matrix of size $Q\times(p+1)$.

Subsequently, X is applied to a randomized autoencoder, and the decoder's learned weights, M, are computed using the Equation 1. These weights contain meaningful spatial and cross-channel related information, as they are trained to decode the randomly encoded color-texture information provided by the 3D sliding cubes. Thus, we define a partial color-texture representation by flattening these learned weights, formulated as:

$$\vec{\Theta}(Q) = \text{flatten}(XZ^T(ZZ^T + \lambda I)^{-1}), \tag{2}$$

where Z, λ and I are the projected matrix, the regularization parameter and the identity matrix, all previously defined in Section 2.1.

Finally, given that the partial representation $\vec{\Theta}(Q)$ relies only on the value of Q, we can enhance our texture representation by combining the learned representations across different Q values. Each distinct Q characterizes the image uniquely, capturing distinct aspects of color and texture. Hence, we define our proposed color-texture representation as:

$$\vec{\Omega}(\mathbf{Q}) = \text{concat}(\vec{\Theta}(Q_1), \vec{\Theta}(Q_2), \ldots, \vec{\Theta}(Q_m)), \tag{3}$$

where $\mathbf{Q} = (Q_1, Q_2, \ldots, Q_m)$.

3 EXPERIMENTS AND RESULTS

3.1 Experimental Setup

In order to evaluate the proposed approach, we used the accuracy metric obtained by employing Linear Discriminant Analysis (LDA) as classifier with the leave-one-out cross-validation strategy. LDA was chosen due to its simplicity, emphasizing that the robustness of the proposed approach stems from the extracted features. Furthermore, we employed three color-texture benchmark datasets with distinct characteristics and variations:

- **USPtex** (Backes et al., 2012): This dataset is composed by 2922 natural texture samples of 128×128 pixels, distributed among 191 classes, each having 12 images.
- **Outex** (Ojala et al., 2002a): Outex consists of 1360 samples partitioned into 68 classes, each having 20 samples of size 128×128 pixels.
- **MBT** (Abdelmounaime and Dong-Chen, 2013): MBT is composed by 2464 texture samples that exhibit distinct intra-band and inter-band spatial patterns. These samples are grouped into 154 classes, each having 16 images of 160×160 pixels.

Finally, we compared our proposed approach with several classical and learning-based approaches reported in the literature. The compared methods include: GLCM (Haralick, 1979), Fourier (Weszka et al., 1976), Fractal (Backes et al., 2009), LBP (Ojala et al., 2002b), LPQ (Ojala et al., 2002b), LCP (Guo et al., 2011), AHP (Zhu et al., 2015), BSIF (Kannala and Rahtu, 2012), CLBP (Guo et al., 2010), LETRIST (Song et al., 2017), LGONBP (Song et al., 2020a), SWOBP (Song et al., 2020b), RNN-RGB (Sá Junior et al., 2019), SSR (Ribas et al., 2024a), VGG11 (Simonyan and Zisserman, 2014), ResNet18 and ResNet50 (He et al., 2016), and DenseNet121 (Huang et al., 2017), and InceptionResNetV2 (Szegedy et al., 2017).

3.2 Parameter Investigation

One of the key advantages of our approach is that it depends solely on a single-type of parameter, which is the number of hidden neurons (Q). This simplicity allows the descriptor to be easily assessed or adapted for other computer vision tasks. Here, we evaluated the proposed descriptor on the three presented texture benchmarks. Specifically, we analyzed the behavior of the classification accuracy (%) of the proposed texture representation $\vec{\Theta}(Q)$ for each dataset, considering the numbers of hidden neurons within the set $\{1, 5, 9, 13, 17, 21, 25, 29\}$, starting from 1 up to 29 in steps of 4.

Figure 3 illustrates that accuracy increases across all datasets as the number of hidden neurons rises, suggesting a positive impact of increasing the number of hidden neurons, Q, of the randomized autoencoder. Nevertheless, at $Q = 21$, the accuracy drops across the datasets, and beyond this point, the accuracy begins to fluctuate, indicating a state of relative stability, particularly for the USPtex and MBT datasets. In summary, these observations imply that our approach benefits from higher-dimensional projections, but overly high dimensions may not be ideal. This behavior could be attributed to the increase in the number of features, to which some datasets, such as Outex, are more sensitive.

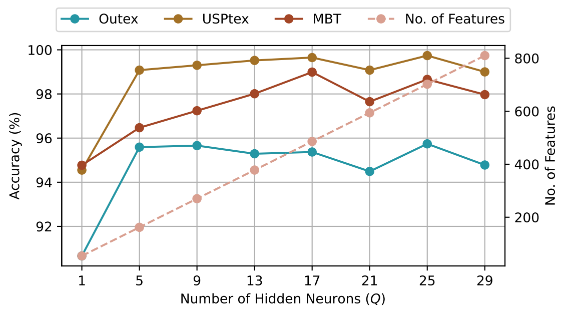

Figure 3: Dynamics of the classification accuracy rate (%) as the number of hidden neurons (Q) rises, for the proposed texture descriptor $\vec{\Theta}(Q)$.

To mitigate fluctuations in the accuracies with a single number of hidden neurons, we combine the texture representations from distinct hidden neurons Q_1 and Q_2. This strategy leverages the diverse textural patterns learned by each neuron to create an even more robust texture descriptor, previously defined as $\vec{\Omega}(Q_1, Q_2)$. We assessed this descriptor by analyzing the accuracy achieved for different combinations of Q_1 and Q_2 of hidden neurons, where $Q_1, Q_2 \in \{1, 5, 9, 13, 17, 21, 25, 29\}$, with $Q_1 < Q_2$.

Table 1 presents the results of the descriptor $\vec{\Omega}(Q_1, Q_2)$ across all datasets, along with the average accuracy. We observed that combining learned representation by varying the number of hidden neurons leads to better accuracy. This finding aligns with other RNN-based investigations, such as (Ribas et al., 2024b; Fares and Ribas, 2024), which showed that combining representations from different latent spaces positively impacts accuracy. This occurs because each learned feature vector uniquely characterizes the textural patterns by learning how to reconstruct them from distinct Q_1- and Q_2-dimensional spaces.

Table 1: Accuracy rates (%) of the proposed descriptor $\vec{\Omega}(Q_1, Q_2)$, for each dataset, and for every possible combination of Q_1 and Q_2. Bold emphasizes the result with highest average accuracy.

(Q_1, Q_2)	# Features	USPtex	Outex	MBT	Avg.
(01, 05)	216	99.0	95.7	97.2	97.3
(01, 09)	324	99.5	96.1	97.9	97.8
(01, 13)	432	99.5	95.4	98.2	97.7
(01, 17)	540	99.6	95.8	98.9	98.1
(01, 21)	648	99.2	94.3	97.7	97.1
(01, 25)	756	99.7	95.9	98.7	98.1
(01, 29)	864	99.1	94.9	98.3	97.4
(05, 09)	432	99.7	96.0	97.3	97.7
(05, 13)	540	99.7	95.2	97.8	97.6
(05, 17)	**648**	**99.6**	**96.0**	**99.1**	**98.2**
(05, 21)	756	99.6	95.2	97.9	97.6
(05, 25)	864	99.6	95.2	98.7	97.8
(05, 29)	972	99.4	96.0	98.3	97.9
(09, 13)	648	99.7	96.1	97.9	97.9
(09, 17)	756	99.7	94.9	98.9	97.8
(09, 21)	864	99.5	94.9	98.3	97.6
(09, 25)	972	99.7	94.9	98.7	97.8
(09, 29)	1080	99.6	95.7	98.4	97.9
(13, 17)	864	99.7	94.9	98.9	97.8
(13, 21)	972	99.7	95.0	98.6	97.8
(13, 25)	1080	99.7	93.8	98.7	97.4
(13, 29)	1188	99.7	95.7	98.4	97.9
(17, 21)	1080	99.7	95.1	99.2	98.0
(17, 25)	1188	99.7	93.2	98.9	97.3
(17, 29)	1296	99.7	95.4	99.2	98.1
(21, 25)	1296	99.7	94.6	98.9	97.8
(21, 29)	1404	99.4	94.8	98.6	97.6
(25, 29)	1512	99.7	95.2	98.9	98.0

Furthermore, although some combinations do not always guarantee improved accuracy, these exceptions could be attributed to the large feature vector sizes, where some datasets such as Outex are more sensitive. This effect is clearly visible in the Outex column, which shows a decline, mainly after the configuration $\vec{\Omega}(09, 13)$, whereas USPtex and MBT maintain a steady performance. Consequently, this trend reveals a peak in the achieved average accuracy, indicating a point where the descriptor offers a robust characterization across all datasets.

Finally, based on these findings, we observed that the configuration $\vec{\Omega}(05, 17)$ achieved the highest average accuracy of 98.2%, making it the most robust version of the proposed approach. Therefore, we selected this configuration for comparison against other methods in the literature.

3.3 Comparison and Discussions

In this section, we compared the previously selected configuration, $\vec{\Omega}(05, 17)$, of our proposed texture approach with methods from the literature described in Section 3.1. The compared methods were evaluated using the same experimental setup: Linear Discriminant Analysis (LDA) with leave-one-out cross-validation, using the accuracy metric for comparison.

Table 2 presents the results obtained by our method and others in the literature. The results highlight that our approach outperformed all compared methods on the USPtex and MBT datasets and achieved the second-best performance on the Outex dataset, surpassed only by SSR (Ribas et al., 2024a). Specifically, when comparing our approach with the classical and RNN-based methods, ranging from GLCM to SSR, our approach not only outperformed SSR by 0.6% on the USPtex dataset but also achieved an accuracy of 99.1% on the MBT dataset, standing out as the only method to surpass the 99% accuracy mark. Furthermore, it is noteworthy that our proposed approach also surpassed other RNN-based methods, such as SSR and RNN-RGB, highlighting the effectiveness of using 3D color cubes to model the multi-channel textural patterns and randomly encode them.

In addition, to provide a broader quantitative analysis, we compared our approach with various deep convolutional neural networks (DCNNs) described in Section 3.1. These networks were used as feature extractors, employing pre-trained models on ImageNet. Furthermore, to prevent excessively large feature vector sizes that could lead to dimensionality issues, features are extracted by applying Global Average Pooling (GAP) to the last convolutional layer, as also done in other investigations, such as (Ribas et al., 2024b).

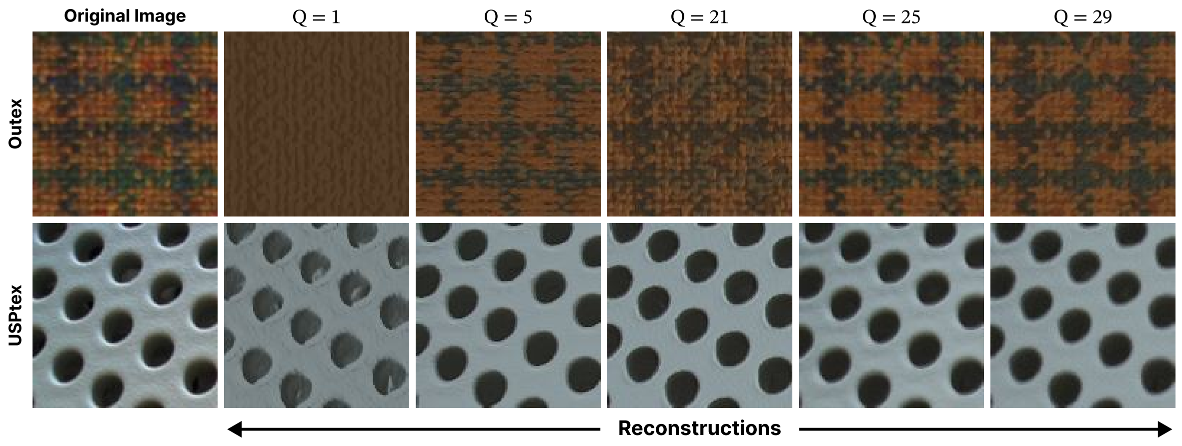

Figure 4: Plot of the original image and their reconstructions for distinct number of hidden neurons (Q). As Q increases the reconstruction quality also improves, with $Q = 25$ being with the most quality from a visual inspection. The quality of the reconstructions suggests that the decoder's learned weights captured the essential texture information.

Table 2: Comparison of the classification accuracy rates (%) of the proposed texture descriptor $\vec{\Omega}(Q_1, Q_2)$ against other methods in the literature on three color-texture datasets. Bold denotes the best result, and underline the second best.

Method	USPTex	Outex	MBT
GLCM integrative	95.9	91.1	97.4
Fourier integrative	91.6	85.8	96.3
Fractal integrative	95.0	86.8	97.0
LBP integrative	90.2	82.4	96.6
LPQ integrative	90.4	80.1	95.7
LCP integrative	96.9	90.7	<u>98.5</u>
AHP integrative	98.7	93.4	98.1
BSIF integrative	82.9	77.9	97.9
CLBP integrative	97.4	89.6	98.2
LGONBP (gray-level)	83.3	83.5	74.2
LETRIST (gray-level)	92.4	82.8	79.1
SWOBP	97.0	79.3	88.3
RNN-RGB	98.4	94.8	–
SSR	99.0	**96.8**	98.0
VGG11	99.3	89.9	93.8
ResNet18	98.7	86.7	90.8
ResNet50	89.4	86.8	85.6
DenseNet121	<u>99.4</u>	84.7	94.1
InceptionResNetV2	96.7	82.4	89.5
Proposed Method			
VCTex	**99.6**	<u>96.0</u>	**99.1**

In this context, Table 2 shows that our proposed method outperformed the DCNN-based approaches across all datasets. Specifically, our approach stands out in both the Outex and MBT datasets, achieving accuracies of 96.0% and 99.1%, respectively. These results correspond to increases of 6.1% on Outex compared to VGG11 (89.9%) and an increase of 5.0% on MBT compared to DenseNet121 (94.1%). These findings suggest that DCNNs face some challenges in characterizing texture on the Outex and MBT, potentially due to micro-texture variations in Outex and inter- and intra-band spatial variations in MBT, whereas our proposed approach efficiently characterizes it. Conversely, although our approach achieved only slight accuracy improvements on USPtex, in comparison to VGG11 (99.3%) and DenseNet121 (99.4%), it still outperformed the compared DCNNs, demonstrating that our method is just as robust for texture characterization as transferred knowledge from models pre-trained on millions of images.

To provide a complement to the quantitative analysis, we assess the qualitative aspect of our approach by plotting their reconstructions, as illustrated in Figure 4. Although we do not use the reconstruction error as a metric for the quantitative aspect of our approach, since we use the decoder's learned weights as texture representation. This figure shows that as the number of hidden neurons increases, Q, the quality of the reconstruction increases, with $Q = 25$ the one most resembling the original image, which matched the best configuration, $\vec{\Theta}(25)$, found in Figure 3. These visualizations are important because they show that the information learned by the decoder's weights carries insightful textural content, indicating the effectiveness of the proposed color-texture representation.

Finally, based on these findings, our proposed approach proved effective in characterizing color textures, outperforming several hand-engineered methods and pre-trained deep convolutional neural networks. These results indicate the robustness of modeling color and textural patterns by sliding 3D color cubes over the image and randomly encoding them, thereby capturing all key color and texture information simultaneously, rather than using gray-scale texture methods applied to each image color channel as integrative approaches do.

3.4 Noise Robustness Analysis

This section assesses the capacity of the proposed texture descriptor regarding noise tolerance. Noise in images is a condition that can happen for some reasons, such as image equipment acquisition. In this context, to evaluate the behavior of the proposed technique in noise conditions, we applied the additive white Gaussian noise (AWGN) to the USPtex dataset with different signal-to-noise ratio (SNR) values specified in decibel (dB). Specifically, we evaluated the compared texture descriptors in the noise-free conditions and in three different SNR $\in \{20, 10, 5\}$, indicating moderate to high levels of noise. Figure 5 shows the noise-free and some noisy samples.

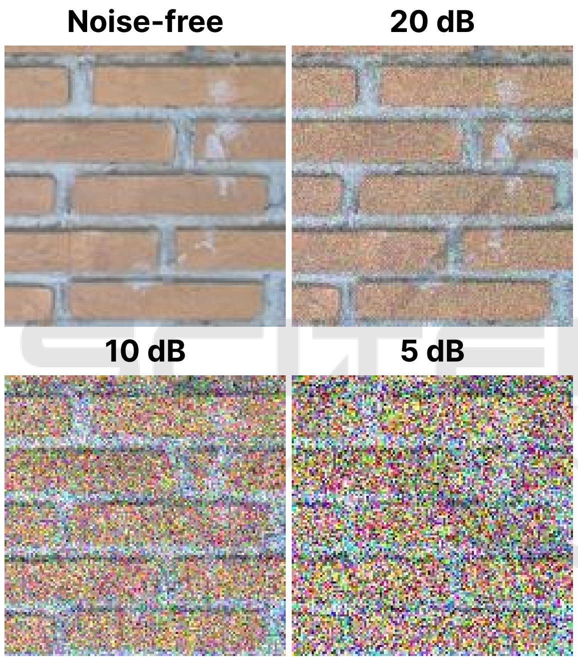

Figure 5: Samples of the USPtex (Backes et al., 2012) dataset in its noise-free condition and with different additive White Gaussian noise conditions specified by the signal-to-noise ratio in decibels (dB).

Table 3 exhibits the comparison of the proposed approach against the compared methods with different SNR values. VCTex achieved the best accuracy in the noise-free condition (99.6%), and the second-best with 20 dB (97.9%), while DenseNet121 achieved the highest one (98.8%). For high levels of noise, VCTex ranked in fourth and fifth for the 10 dB (81.7%) and 5 dB (60.7%) conditions, respectively. These results indicate that VCTex is tolerant for a moderate level of noise, and although it did not achieve the highest accuracies in high level conditions, it remained in the top five.

Therefore, based on the results, we suspect that the sensitivity of VCTex in high levels of noise is due to the direct encoding of image pixel intensities through $3 \times 3 \times 3$ cubes. Under high-noise conditions, these pixels are significantly modified, leading the proposed texture representation to encode some of the noise. This is somehow undesirable for learning a robust texture representation. This hypothesis is further supported by the better noise tolerance demonstrated by SSR, a method that encodes pixels using a graph-based model. Consequently, VCTex exhibits certain limitations when dealing with excessive noise levels.

Table 3: Comparison of the accuracy rates (%) of the proposed texture descriptor against other literature methods in distinct additive white Gaussian noise (AWGN) conditions specified by the signal-to-noise ratio value in decibels (dB).

		AWGN		
Method	Noise-free	20 dB	10 dB	5 dB
GLCM integrative	95.9	91.0	71.6	55.2
Fourier integrative	91.6	85.2	70.4	61.8
Fractal integrative	95.0	73.8	46.4	31.8
LBP integrative	90.2	66.8	32.7	28.2
LPQ integrative	90.4	78.8	43.2	23.7
LCP integrative	96.9	86.8	61.5	51.8
AHP integrative	98.7	90.0	70.5	58.1
BSIF integrative	82.9	76.1	52.1	33.3
CLBP integrative	97.4	42.5	21.0	17.5
LGONBP (gray-level)	92.4	77.7	55.1	35.6
LETRIST (gray-level)	97.0	87.5	64.8	43.1
SWOBP	98.4	86.0	55.4	40.2
SSR	99.0	97.9	86.4	**68.8**
VGG11	99.3	95.7	71.3	39.1
ResNet18	98.7	96.8	80.1	51.8
ResNet50	89.4	86.3	53.8	34.5
DenseNet121	99.4	**98.8**	**88.9**	65.6
InceptionResNetV2	96.7	97.0	85.7	62.0
Proposed Approach				
VCTex	**99.6**	97.9	81.7	60.7

3.5 Computational Efficiency

In this analysis, we investigate how computationally efficient the proposed approach is against the compared methods in the literature. For this purpose, we compared the average running time of the feature extraction methods in 100 trials after 10 warm-up trials. These warm-up trials were employed to prevent some outlier measurements, such as those caused by cold start issues. Therefore, doing so allowed us to provide a more robust and consistent analysis of the results.

To run the processing time measurement experiments, we used a server equipped with a i9-14900KF processor with 128 GB RAM and a GeForce RTX 4090 24GB GPU, running on the Ubuntu 22.04 operating system. The hand-engineered methods and SSR were implemented using MATLAB (R2023b), while the DCNN-based methods and VCTex were implemented using Python v3.11.9 and the PyTorch (Paszke et al., 2019) library v2.4.0.

Table 4 presents the average processing time (in seconds) for the compared hand-engineered methods. As shown, our proposed approach (VCTex) achieved the lowest average processing time of 0.0093 seconds (9.3 ms), exhibiting a very efficient approach. Further, in comparison, our approach is 1.95× faster than the second most efficient approach (LBP), and also achieved superior classification results across all benchmark datasets as presented in Table 2. Additionally, regarding other RNN-based techniques, such as SSR, our approach demonstrated to be 242× faster. Here, although SSR uses the RNN architecture (which is simple and fast), this high cost in processing time is largely due to the graph-modeling phase.

Table 4: Report of the average processing time (in seconds) of 100 trials for each compared hand-engineered method using a 224×224 RGB image. Bold denotes the best result, and underline the second best. Lower values are preferable.

Method	CPU Time (s)
GLCM integrative	0.0421 ± 0.0082
Fourier integrative	0.0553 ± 0.0089
Fractal integrative	2.8410 ± 0.0085
LBP integrative	0.0181 ± 0.0075
LPQ integrative	0.2302 ± 0.0154
LCP integrative	0.1176 ± 0.0105
AHP integrative	0.1746 ± 0.0126
BSIF integrative	0.0295 ± 0.0085
CLBP integrative	0.2366 ± 0.0156
LGONBP (gray-level)	0.3839 ± 0.0214
LETRIST (gray-level)	0.0246 ± 0.0035
SWOBP	0.3198 ± 0.0453
SSR	2.2551 ± 0.0971
Proposed Approach	
VCTex	**0.0093** ± **0.0002**

Following this, Table 5 shows the average processing time (in seconds) in both CPU and GPU for the DCNN-based methods in comparison to VCTex. In terms of CPU time, the VCTex achieved the lowest average processing time (9.3 ms), being faster than the compared architectures in 2.83× (VGG11), 1.51× (ResNet18), 2.96× (ResNet50), 57.03× (DenseNet121) and 6.94× (InceptionResNetV2). Conversely, in terms of GPU time, the lowest average processing time was achieved by VGG11 with 0.0004 seconds (0.4 ms), and the second best was achieved by ResNet18 with 0.0010 seconds (1.0 ms), with our approach ranking in third with 0.0013 seconds (1.3 ms). Although the VCTex is slightly slower than ResNet18 and 3.25× slower than VGG11, our proposed method consistently outperformed these pre-trained feature extractors in all the benchmark datasets, thus showing a good balance between the trade-off of computational efficiency and accuracy.

Table 5: Report of the average processing time (in seconds) of 100 trials for each compared DCNN-based method using a 224×224 RGB image. Bold denotes the best result, and underline the second best. Lower values are preferable.

	Time (ms)	
Method	CPU	GPU
VGG11	0.0263 ± 0.0007	**0.0004** ± **0.0001**
ResNet18	0.0140 ± 0.0007	0.0010 ± 0.0000
ResNet50	0.0275 ± 0.0006	0.0025 ± 0.0000
DenseNet121	0.5304 ± 0.0225	0.0065 ± 0.0000
InceptionResNetV2	0.0645 ± 0.0005	0.0124 ± 0.0001
Proposed Approach		
VCTex	**0.0093** ± **0.0002**	0.0013 ± 0.0000

Therefore, this investigation showed that VCTex has a high competitive computational performance, achieving the lowest average processing in CPU time across all compared methods, and ranking in third in terms of GPU time. This good performance is largely due to the employed RNN architecture and the rapid tensor stride manipulation operations to obtain the $3 \times 3 \times 3$ cubes across every pixel in the image. In this sense, VCTex presents as a competitive approach both in terms of accuracy and computational performance.

3.6 Classification of Colorectal Polyps

Colorectal cancer (CRC) is the second leading cause of cancer-related mortality and the third most frequently diagnosed cancer worldwide (Choe et al., 2024). Thus, early diagnosis is important, as it allows for early treatment initiation, increasing the chances of recovery. In this sense, with the continued growth and advancement of machine learning techniques, numerous methods are being applied to medical diagnosis as auxiliary decision-support tools. Therefore, we assessed the applicability of the proposed approach in the challenging task of classifying colorectal polyps.

To this end, we used the MHIST (Wei et al., 2021) dataset, designed to classify colorectal polyps as benign or precancerous, as a benchmark application for the proposed technique. The dataset consists of 3,152 hematoxylin and eosin (H&E)-stained patches, each sized 224×224 pixels, extracted from 328 whole slide images (WSIs) scanned at 40× resolution. The patches are labeled as Hyperplastic Polyp (HP) or Sessile Serrated Adenoma (SSA). The difficulty of this dataset arises from the significant inter-pathologist disagreement in diagnosing HP and SSA. The gold-standard labels were assigned based on the majority vote of seven board-certified pathologists.

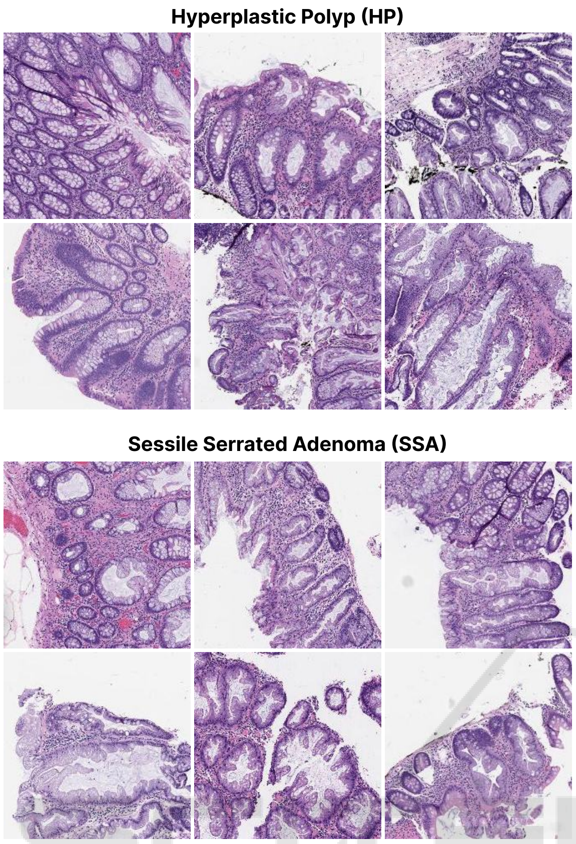

Figure 6: Samples of the MHIST (Wei et al., 2021) dataset. The first two rows of images corresponds to samples of Hyperplastic Polyp (HP) a typically benign growths, and the last two ones correspond to Sessile Serrated Adenoma (SSA), a precancerous lesion.

Figure 6 presents HP and SSA samples of MHIST.

For the experimental setup, Linear Discriminant Analysis (LDA) was used as the classifier, utilizing the pre-defined training and test splits of the MHIST dataset, consisting of 2,175 and 977 samples, respectively. Furthermore, we used four metrics for evaluation: accuracy, precision, recall, and F-score, due to their importance in medical applications.

In the experimentation, we evaluated the behavior of our proposed texture descriptor, $\vec{\Theta}(Q)$ and $\vec{\Omega}(Q_1, Q_2)$, by analyzing all possible parameter combinations, as outlined in Section 3.2. Figure 7 presents a heatmap of the achieved accuracies. The main diagonal contains the results for the descriptor $\vec{\Theta}(Q)$, since $Q_1 = Q_2$, while the off-diagonal entries show the accuracies for the representation $\vec{\Omega}(Q_1, Q_2)$. The heatmap revealed that configurations involving combinations of higher-dimensional projections, $\vec{\Omega}(Q_1, Q_2)$, did not result in high accuracies, probably due to the large size of their feature vectors. This is evident in the region of Figure 7 delimited by $Q_1 \in \{13, 17, 21\}$ and $Q_2 \in \{21, 25, 29\}$, which shows a bluer area. In contrast, the proposed descriptor $\vec{\Theta}(Q)$ which does not combine multiple representations, and the descriptor $\vec{\Omega}(Q_1, Q_2)$ when combining low-dimensional projections achieved the highest accuracies, such as $\vec{\Theta}(25)$ and $\vec{\Omega}(01, 25)$, which achieved accuracies of 73.4% and 72.7%, respectively. Therefore, we selected the simple, compact texture descriptor $\vec{\Theta}(25)$ which achieved the highest accuracy of 73.4%, to be compared with other literature methods.

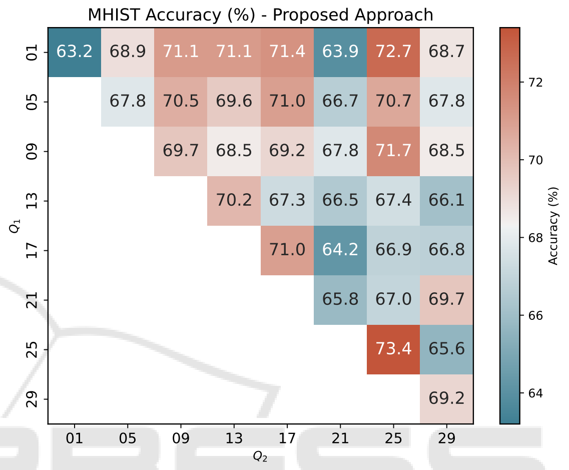

Figure 7: Accuracy rates (%) on MHIST dataset for the proposed approach. The main diagonal corresponds to the $\vec{\Theta}(Q)$ descriptor, since $Q_1 = Q_2$. The accuracies on the off-diagonal corresponds to the $\vec{\Omega}(Q_1, Q_2)$ descriptor.

In Table 6, we presented the comparison of our proposed approach against other methods in the literature. The results show that the proposed approach outperformed all other texture-related methods in relation to accuracy and precision, while ranking second for recall and F-score. Compared to another randomized neural network-based approach (SSR), our method surpassed it by 4.8% in accuracy, corresponding to 47 additional correctly classified images. This result demonstrates the effectiveness of sliding 3D color cubes over the images to capture both spatial (texture) and color (spectral) patterns.

Additionally, we also compared our approach with various pre-trained deep convolutional neural networks used as feature extractors. In particular, our approach achieved higher accuracy and precision than all compared DCNNs, including VGG11 (0.4%), ResNet18 (0.4%), ResNet50 (13.8%), DenseNet121 (0.9%), and InceptionResNetV2 (4.5%), where the values in parentheses denote the accuracy improvement of our approach over each DCNN.

Still, although our method ranks second in recall

Table 6: Comparison of classification accuracies of different literature methods for the very challenging task of classification of colorectal polyps on the MHIST dataset. Bold denotes the best result, and underline the second best.

Method	Accuracy	Precision	Recall	F-score
GLCM integrative	65.0	61.3	59.2	59.2
Fourier integrative	65.5	62.1	60.5	60.8
Fractal integrative	65.7	62.5	61.3	61.6
LBP integrative	60.1	56.7	56.5	56.6
LPQ integrative	63.1	59.6	58.9	59.0
LCP integrative	68.4	65.7	62.7	63.0
AHP integrative	65.3	62.0	60.8	61.0
BSIF integrative	63.7	60.8	60.6	60.7
CLBP integrative	54.8	54.0	54.2	53.5
LGONBP (gray-level)	62.7	60.0	60.1	60.1
LETRIST (gray-level)	68.5	65.7	63.6	64.0
SWOBP	67.5	64.5	62.4	62.8
SSR	68.6	66.1	65.7	65.9
VGG11	73.0	70.9	70.3	70.6
ResNet18	73.0	71.0	**71.2**	**71.1**
ResNet50	59.6	58.9	59.5	58.5
DenseNet121	72.5	70.5	70.6	70.5
InceptionResNetV2	68.9	66.9	67.3	67.0
Proposed Method				
VCTex	**73.4**	**71.4**	70.6	70.9

and F-score, with ResNet18 achieving the highest values, improving by 0.6% in recall and 0.2% in F-score, it is noteworthy that our approach produced competitive results compared to these DCNNs pre-trained on millions of images, highlighting the robustness of our simple, fast and low computational cost approach, in comparison to these larger and expensive DCNNs architectures.

Finally, the results demonstrate that our method outperformed all compared texture methods in accuracy, including pre-trained deep convolutional neural networks used as feature extractors. This result highlights the effectiveness of our approach in the very challenging and important task of classifying colorectal polyps. These findings suggest that our method could be further explored to other histological image problems, offering a simple and cost-effective solution.

4 CONCLUSIONS

In this paper, we proposed a new color-texture representation based on randomized autoencoder that simultaneously encodes texture and color information using volumetric (3D) color cubes. For each image, a 3D color cube slides over the image, capturing both texture and color (spectral) patterns. These patterns are then encoded by the randomized autoencoder, and we use as color-texture representation the flattened weights of the decoder's learned weights. The effectiveness of our approach is evidenced by the results on color-texture datasets, where our method outperformed several methods from the literature, including deep convolutional neural networks.

Moreover, we show the applicability and robustness of the proposed approach in the challenging and important task of colorectal polyp classification, aiding the identification of colorectal cancer using only texture-related information. Therefore, this study shows the effectiveness of random encoding color-texture information using volumetric (3D) color cubes, culminating in a simple, fast, and efficient approach. As future work, this method may be adapted to hyperspectral images, dynamic textures, or alternative strategies for encoding color cube information.

ACKNOWLEDGEMENTS

R. T. Fares acknowledges support from FAPESP (grant #2024/01744-8), L. C. Ribas acknowledges support from FAPESP (grants #2023/04583-2 and 2018/22214-6). This study was financed in part by the Coordenação de Aperfeiçoamento de Pessoal de Nível Superior - Brasil (CAPES).

REFERENCES

Abdelmounaime, S. and Dong-Chen, H. (2013). New brodatz-based image databases for grayscale color and multiband texture analysis. *International Scholarly Research Notices*, 2013.

Backes, A. R., Casanova, D., and Bruno, O. M. (2009). Plant leaf identification based on volumetric fractal dimension. *International Journal of Pattern Recognition and Artificial Intelligence*, 23(06):1145–1160.

Backes, A. R., Casanova, D., and Bruno, O. M. (2012). Color texture analysis based on fractal descriptors. *Pattern Recognition*, 45(5):1984–1992.

Backes, A. R., Casanova, D., and Bruno, O. M. (2013). Texture analysis and classification: A complex network-based approach. *Information Sciences*, 219:168–180.

Calvetti, D., Morigi, S., Reichel, L., and Sgallari, F. (2000). Tikhonov regularization and the l-curve for large discrete ill-posed problems. *Journal of Computational and Applied Mathematics*, 123(1):423–446.

Choe, A. R., Song, E. M., Seo, H., Kim, H., Kim, G., Kim, S., Byeon, J. R., Park, Y., Tae, C. H., Shim, K.-N., et al. (2024). Different modifiable risk factors for the development of non-advanced adenoma, advanced adenomatous lesion, and sessile serrated lesions, on screening colonoscopy. *Scientific Reports*, 14(1):16865.

Cover, T. M. (1965). Geometrical and statistical properties of systems of linear inequalities with applications in pattern recognition. *IEEE Transactions on Electronic Computers*, EC-14(3):326–334.

Deng, J., Dong, W., Socher, R., Li, L.-J., Li, K., and Fei-Fei, L. (2009). Imagenet: A large-scale hierarchical image database. In *2009 IEEE conference on computer vision and pattern recognition*, pages 248–255. Ieee.

Fares, R. T. and Ribas, L. C. (2024). Randomized autoencoder-based representation for dynamic texture recognition. In *2024 31st International Conference on Systems, Signals and Image Processing (IWSSIP)*, pages 1–7. IEEE.

Fares, R. T., Vicentim, A. C. M., Scabini, L., Zielinski, K. M., Jennane, R., Bruno, O. M., and Ribas, L. C. (2024). Randomized encoding ensemble: A new approach for texture representation. In *2024 31st International Conference on Systems, Signals and Image Processing (IWSSIP)*, pages 1–8. IEEE.

Guo, Y., Zhao, G., and Pietikäinen, M. (2011). Texture classification using a linear configuration model based descriptor. In *BMVC*, pages 1–10. Citeseer.

Guo, Z., Zhang, L., and Zhang, D. (2010). A completed modeling of local binary pattern operator for texture classification. *IEEE Transactions on Image Processing*, 19(6):1657–1663.

Haralick, R. M. (1979). Statistical and structural approaches to texture. *Proceedings of the IEEE*, 67(5):786–804.

He, K., Zhang, X., Ren, S., and Sun, J. (2016). Deep residual learning for image recognition. In *Proceedings of the IEEE conference on computer vision and pattern recognition*, pages 770–778.

Hu, S., Li, J., Fan, H., Lan, S., and Pan, Z. (2024). Scale and pattern adaptive local binary pattern for texture classification. *Expert Systems with Applications*, 240:122403.

Huang, G., Liu, Z., Van Der Maaten, L., and Weinberger, K. Q. (2017). Densely connected convolutional networks. In *Proceedings of the IEEE conference on computer vision and pattern recognition*, pages 4700–4708.

Huang, G.-B., Zhu, Q.-Y., and Siew, C.-K. (2006). Extreme learning machine: Theory and applications. *Neurocomputing*, 70(1):489–501.

Kannala, J. and Rahtu, E. (2012). Bsif: Binarized statistical image features. In *Pattern Recognition (ICPR), 2012 21st International Conference on*, pages 1363–1366. IEEE.

Krizhevsky, A., Sutskever, I., and Hinton, G. E. (2012). ImageNet Classification with Deep Convolutional Neural Networks. *Advances In Neural Information Processing Systems*, pages 1–9.

Li, L., Yao, Z., Gao, S., Han, H., and Xia, Z. (2024). Face anti-spoofing via jointly modeling local texture and constructed depth. *Engineering Applications of Artificial Intelligence*, 133:108345.

Liu, G.-H. and Yang, J.-Y. (2023). Exploiting deep textures for image retrieval. *International Journal of Machine Learning and Cybernetics*, 14(2):483–494.

Marinó, G. C., Petrini, A., Malchiodi, D., and Frasca, M. (2023). Deep neural networks compression: A comparative survey and choice recommendations. *Neurocomputing*, 520:152–170.

Moore, E. H. (1920). On the reciprocal of the general algebraic matrix. *Bulletin of American Mathematical Society*, pages 394–395.

Ojala, T., Mäenpää, T., Pietikäinen, M., Viertola, J., Kyllönen, J., and Huovinen, S. (2002a). Outex - new framework for empirical evaluation of texture analysis algorithms. *Object recognition supported by user interaction for service robots*, 1:701–706 vol.1.

Ojala, T., Pietikainen, M., and Maenpaa, T. (2002b). Multiresolution gray-scale and rotation invariant texture classification with local binary patterns. *IEEE Transactions on pattern analysis and machine intelligence*, 24(7):971–987.

Pao, Y.-H., Park, G.-H., and Sobajic, D. J. (1994). Learning and generalization characteristics of the random vector functional-link net. *Neurocomputing*, 6(2):163–180.

Pao, Y.-H. and Takefuji, Y. (1992). Functional-link net computing: theory, system architecture, and functionalities. *Computer*, 25(5):76–79.

Paszke, A., Gross, S., Massa, F., Lerer, A., Bradbury, J., Chanan, G., Killeen, T., Lin, Z., Gimelshein, N., Antiga, L., Desmaison, A., Kopf, A., Yang, E., DeVito, Z., Raison, M., Tejani, A., Chilamkurthy, S., Steiner, B., Fang, L., Bai, J., and Chintala, S. (2019). PyTorch: An Imperative Style, High-Performance Deep Learning Library. In *Advances in Neural Information Processing Systems 32*, pages 8024–8035. Curran Associates, Inc.

Penrose, R. (1955). A generalized inverse for matrices. *Mathematical Proceedings of the Cambridge Philosophical Society*, 51(3):406–413.

Rangaiah, P. K., Augustine, R., et al. (2025). Improving burn diagnosis in medical image retrieval from grafting burn samples using b-coefficients and the clahe algorithm. *Biomedical Signal Processing and Control*, 99:106814.

Ribas, L. C., Scabini, L. F., Condori, R. H., and Bruno, O. M. (2024a). Color-texture classification based on spatio-spectral complex network representations. *Physica A: Statistical Mechanics and its Applications*, page 129518.

Ribas, L. C., Scabini, L. F., de Mesquita Sá Junior, J. J., and Bruno, O. M. (2024b). Local complex features learned by randomized neural networks for texture analysis. *Pattern Analysis and Applications*, 27(1):1–12.

Sá Junior, J. J. d. M. and Backes, A. R. (2016). Elm based signature for texture classification. *Pattern Recognition*, 51:395–401.

Sá Junior, J. J. d. M., Backes, A. R., and Bruno, O. M. (2019). Randomized neural network based signature for color texture classification. *Multidimensional Systems and Signal Processing*, 30(3):1171–1186.

Scabini, L. F., Condori, R. H., Gonçalves, W. N., and Bruno, O. M. (2019). Multilayer complex network descriptors for color–texture characterization. *Information Sciences*, 491:30–47.

Schmidt, W., Kraaijveld, M., and Duin, R. (1992). Feedforward neural networks with random weights. In *Proceedings., 11th IAPR International Conference on*

Pattern Recognition. Vol.II. Conference B: Pattern Recognition Methodology and Systems, pages 1–4.

Simonyan, K. and Zisserman, A. (2014). Very deep convolutional networks for large-scale image recognition. *CoRR*, abs/1409.1556.

Song, T., Feng, J., Luo, L., Gao, C., and Li, H. (2020a). Robust texture description using local grouped order pattern and non-local binary pattern. *IEEE Transactions on Circuits and Systems for Video Technology*, 31(1):189–202.

Song, T., Feng, J., Wang, S., and Xie, Y. (2020b). Spatially weighted order binary pattern for color texture classification. *Expert Systems with Applications*, 147:113167.

Song, T., Li, H., Meng, F., Wu, Q., and Cai, J. (2017). Letrist: Locally encoded transform feature histogram for rotation-invariant texture classification. *IEEE Transactions on circuits and systems for video technology*, 28(7):1565–1579.

Su, Y., Yan, P., Lin, J., Wen, C., and Fan, Y. (2024). Few-shot defect recognition for the multi-domain industry via attention embedding and fine-grained feature enhancement. *Knowledge-Based Systems*, 284:111265.

Szegedy, C., Ioffe, S., Vanhoucke, V., and Alemi, A. A. (2017). Inception-v4, inception-resnet and the impact of residual connections on learning. In *Thirty-First AAAI Conference on Artificial Intelligence*.

Tikhonov, A. N. (1963). On the solution of ill-posed problems and the method of regularization. *Dokl. Akad. Nauk USSR*, 151(3):501–504.

Wang, Y., Huang, G., Song, S., Pan, X., Xia, Y., and Wu, C. (2021). Regularizing deep networks with semantic data augmentation. *IEEE Transactions on Pattern Analysis and Machine Intelligence*, 44(7):3733–3748.

Wei, J., Suriawinata, A., Ren, B., Liu, X., Lisovsky, M., Vaickus, L., Brown, C., Baker, M., Tomita, N., Torresani, L., et al. (2021). A petri dish for histopathology image analysis. In *International Conference on Artificial Intelligence in Medicine*, pages 11–24. Springer.

Weszka, J. S., Dyer, C. R., and Rosenfeld, A. (1976). A comparative study of texture measures for terrain classification. *IEEE transactions on Systems, Man, and Cybernetics*, (4):269–285.

Zhu, Z., You, X., Chen, C. P., Tao, D., Ou, W., Jiang, X., and Zou, J. (2015). An adaptive hybrid pattern for noise-robust texture analysis. *Pattern Recognition*, 48(8):2592–2608.